Chapter 4

Effect of Zn^{2+} co-doping on the luminescence of Sm^{3+} doped $SrMoO_4$ phosphor

In this chapter, we discuss the result of Zn^{2+} co-doping on the photoluminescence and structural properties of Sm^{3+} doped $SrMoO_4$ phosphors. The structural study ascertains the improvement in crystallinity of the Sm^{3+} doped $SrMoO_4$ phosphor by Zn^{2+} co-doping. PL excitation analysis evinces that the intensity of 404 nm peak ($^6H_{5/2} \rightarrow {}^4F_{7/2}$) is enhanced by 93.5% after 1% Zn^{2+} co-doping in the 4% Sm^{3+} doped $SrMoO_4$ phosphor. The reddish-orange emission intensity of 4% Sm^{3+} doped $SrMoO_4$ is further increased by 87.80% after 1% Zn^{2+} co-doping. The temperature-dependent emission spectra reveal good thermal stability of the phosphor. The prepared Zn^{2+} co-doped SrMoO4:4Sm^{3+} phosphor has near-UV excitation and reddish-orange emission and thus can be used as a potential red phosphor in lighting devices.

4.1 Introduction

In chapter 3 we have studied Bi^{3+}/Sm^{3+} co-doped $SrMoO_4$ red phosphor for wLED application. It was shown that the $SrMoO_4$ phosphor is a self-activated luminescent phosphor having near UV absorption and greenish-blue emission due to the electron transfer between O^{2-} and Mo^{6+} in $[MoO_4]^{2-}$ groups. The doping of Sm^{3+} ions gives reddish-orange emission and the emission intensity of the Sm^{3+} ion can be enhanced by co-doping Bi^{3+} ions as it assists the crystallite size growth, thereby improving the crystallinity of the phosphor.

It is known that the emission intensity of RE ions can also be increased by co-doping different alkali (Li^+, K^+, Na^+) and transition metals (Mn^{2+}, Zn^{2+}, etc) [113,141,142]. These foreign ions easily occupy the substitutional or interstitial sites due to their relatively small ionic radius. These ions influence the crystal field around the RE ion by increasing the asymmetry. These ions also improve crystallinity and reduce defect states. All of these effects help in improving the luminescence intensity of RE ions. In this chapter, we examine the effect of Zn^{2+} ions on the optical and structural properties of Sm^{3+} doped $SrMoO_4$ synthesized by the lucrative auto-combustion process for the first time.

The Zn^{2+}/Sm^{3+} codoped $SrMoO_4$ phosphors studied in this chapter can be utilized as a red-emitting source for white LEDs applications. White LEDs, as we know have succeeded fluorescent lamps owing to their prominent advantages such as environmental friendliness, energy efficacy, enhanced optical power, longer operating lifetime, and high luminous efficacy. Currently, commercial wLEDs are fabricated by coating Ce^{3+}:YAG yellow phosphor over the blue chips to emit white light [53,91]. However, the white light emitted by this combination lacks sufficient power distribution in the red spectral region, which leads to high correlated color temperature (CCT > 4,500 K) and a limited color rendering index

(CRI<75) [58]. To overcome this problem, the tricolor (RGB) phosphors can be used for the realization of white light emission but this technique suffers from several limitations such as re-absorption of light, color ratio adjustment, and radiant inefficiency. The other way is by using red phosphors and yellow phosphors [54–58]. However, a significant part of the emitted light of these phosphors lies outside the human eye spectral sensitivity range (i.e. beyond 700 nm), which limits their use in the wLED application. Other limitations of these phosphors, such as the requirement of high temperature and reduced atmosphere for synthesis lead to heavy financing and hinder their practical applications. Therefore, a chemically and thermally stable red-emitting phosphor that can be developed by an environmentally friendly and low-cost synthesis process is desired for the wLED application and in this regard, our studied Zn^{2+}/Sm^{3+} codoped $SrMoO_4$ phosphors can be helpful.

4.2. Methods

4.2.1 Preparation of phosphors

The initial precursors for the synthesis were ammonium molybdate (para) tetrahydrate, strontium oxide, samarium nitrate, and zinc nitrate hexahydrate. The Sm^{3+} (0%, 1%, 3%, 4%, 5%) doped $SrMoO_4$ and Zn^{2+} (1%, 2%, and 3%) co-doped in 4% Sm^{+3} doped $SrMoO_4$ phosphor are coded as S0, S1, S3, S4, S5, Z1, Z2, and Z3, respectively. The samples were prepared by a lucrative urea-assisted auto combustion method as discussed in chapter 2. Fig.4.1 presents the schematic of the synthesis process.

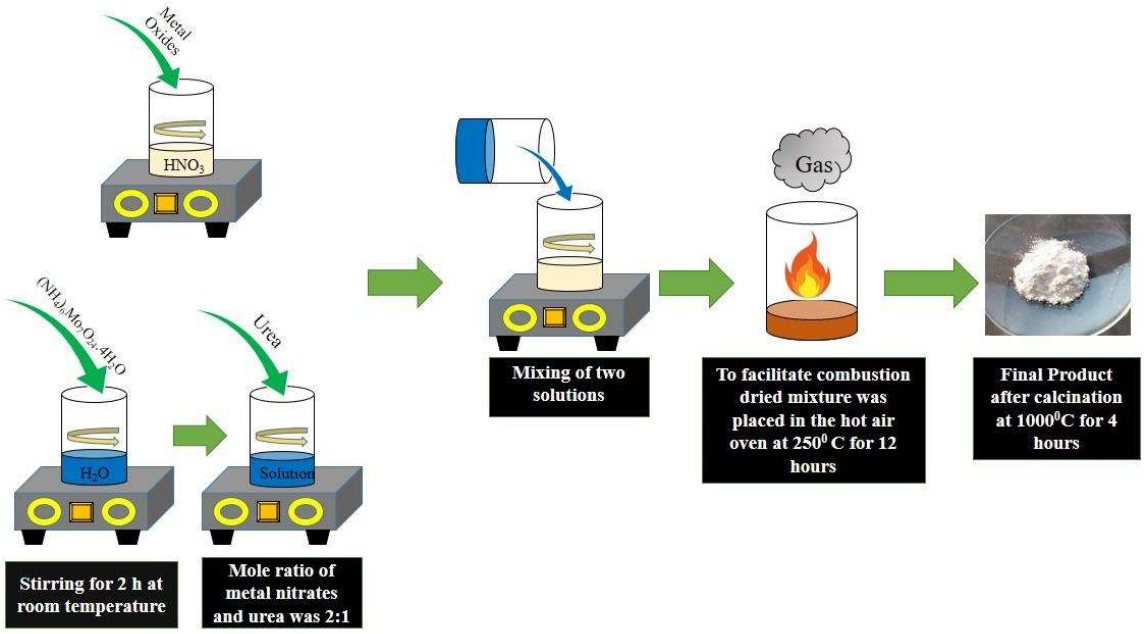

Fig. 4.1 Schematic describing the synthesis process.

4.2.2 Characterization techniques

The X-ray diffraction (XRD) data were recorded with the help of a Rigaku-Mini FlexII DESKTOP powder X-ray diffractometer having Cu K_α (λ=1.54Å) as a radiation source. The phase purity and crystal structure was validated by the use of FULLPROF software [119]. A scanning electron microscope (SEM) is used to get micrographs of the phosphors (Nova Nano SEM 450, FEI). The average particle was calculated using ImageJ computer software. The vibrational modes of the phosphors were determined from FTIR scans, obtained using a JASCO FT/IR 4600 spectrometer coupled with the Attenuated total reflection (ATR) setup, which consists of a diamond disc as an internal reflection element. The JASCO V770 UV-Vis-NIR spectrophotometer was used to perform the absorption analysis. The Photoluminescence excitation (PLE) and emission (PL) analysis was done using a Horiba Fluorolog-3 spectrophotometer with a xenon flash lamp (450w) as an excitation source. The PL and PLE spectrum of all the prepared phosphors were obtained for the slit width fixed at 1 nm. The PL lifetime measurement was done using the FLS920 Fluorescence spectrometer (Edinburgh Instruments) equipped with a 60W xenon flash lamp. Thermo

Fischer Scientific ESCALAB Xi X-ray photoelectron spectrometer was used for XPS measurements. The temperature-dependent PL (TDPL) measurements were performed using an assembly containing a spectrophotometer (Ocean Optics) with a diode laser (405 nm) as an excitation source and an optical furnace to heat the phosphor.

4.3. Results and discussion

4.3.1 XRD study

Fig. 4.2 (a) represents the Rietveld refined XRD patterns of S0, S4, and Z1 phosphors scanned over the $20^o \leq 2\theta \leq 80^o$ range. The XRD graph substantiates the tetragonal crystal structure of the phosphors having $I4_1/a$ space group. The prominent peaks such as (112), (004), (200), (211), (204), (220), (116), (312), and (136) are found in concurrence with the standard JCPDS file No. 08-0482 (a=b=5.394 Å and c=12.020 Å) [20,143]. The Sm^{3+} (1.079 Å) and Zn^{2+} (0.90 Å) ions are expected to be substituted in Sr^{2+} (1.26 Å) site as the ionic radius of Sm^{3+} and Zn^{2+} for the system having coordination number = 8 is nearer to Sr^{2+} (1.26 Å) [144]. The tetragonal crystal structure of $SrMoO_4$ obtained after refinement of the XRD pattern is presented in Fig. 4.2 (b). The $SrMoO_4$ structure is formed by SrO_8 dodecahedral and MoO_4 tetrahedron attached by Sr–O–Mo bonds [24]. The values of atomic positions, lattice parameters, and unit cell volume of S0, S4, and Z1 phosphors which are obtained using FULLPROF software are listed in Table 4.1 [119]. The lattice parameters decrease by doping Sm^{3+} and Zn^{2+} ions, which is the result of the difference in ionic radius of Sr^{2+} and the dopants. The change in lattice parameters suggests that the dopants (Sm^{3+} and Zn^{2+}) have been integrated into the Sr^{2+} site of the $SrMoO_4$ structure [23,24]. The reduction in lattice parameters causes volume of the unit cell to contract.

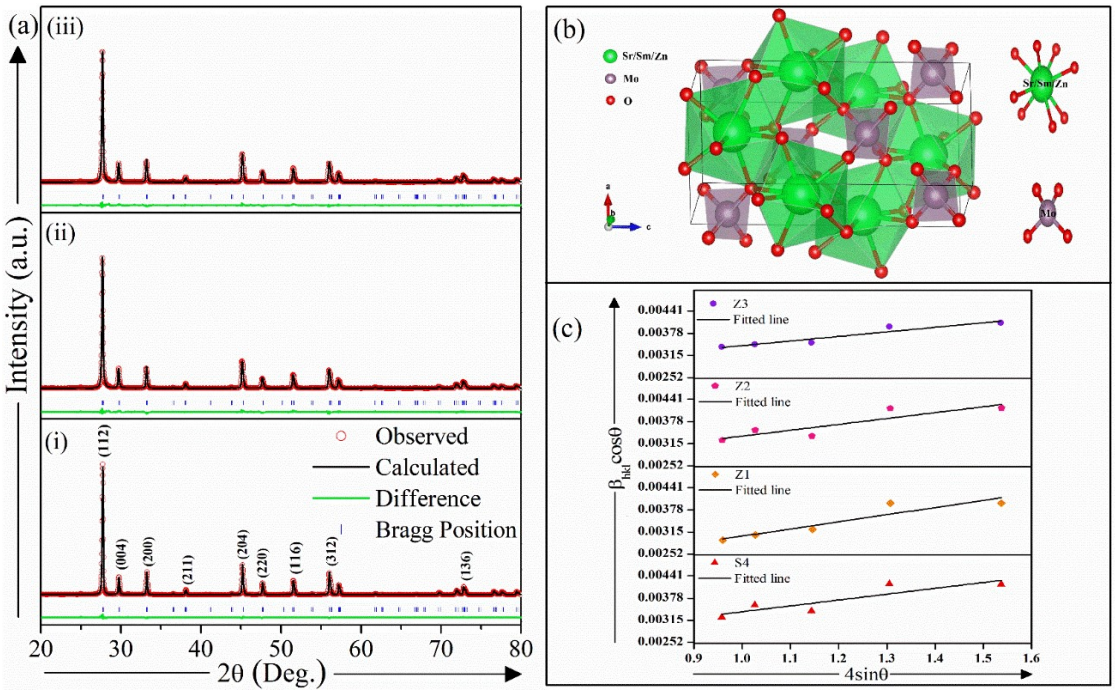

Fig. 4.2 (a) Rietveld refined XRD patterns of **(i)** S0, **(ii)** S4, and **(iii)** Z1 phosphors. **(b)** The tetragonal crystal structure of $SrMoO_4$. **(c)** The linearly fitted W-H plots of S4, Z1, Z2, and Z3.

The expression in equation (4.1) of the Williamson-Hall (W-H) method is used to evaluate the crystallite size (d) and microstrain (ϵ) in the lattice [23,141],

$$\beta cos\theta = 4\epsilon sin\theta + \frac{k\lambda}{d}, \tag{4.1}$$

Where β is the full width at half maximum (FWHM) which is calculated after subtracting instrumental broadening ($\beta_{instrumental}$) from the FWHM ($\beta_{measured}$) of diffraction peak, θ represents the diffraction peak angle, λ is the wavelength (0.154 nm for Cu Kα) used, and k is the shape factor (k~ 0.9) [23,141]. The linearly fitted W-H plots of S4, Z1, Z2, and Z3 are presented in Fig. 4.2 (c). The crystallite size (d) is obtained from the intercept of the linearly fitted line. The obtained values of the d are listed in Table 4.2. It is perceived that a small percentage of Zn^{2+} (1%) co-doping helps in increasing the crystallite size of the phosphor but on further co-doping of Zn^{2+}, the value d is decreased due to interstitial occupancy of Zn^{2+} ions at higher concentration. The increase in d for Z1 phosphor is the

indication of the improved crystallinity [121,142]. The grain boundaries adsorb the photons generated in the microcrystals but they are reduced with the increase in crystallite size and hence, increased crystallinity is favorable for luminescence enhancement [121,142].

Table 4.1 Atomic positions, lattice parameters, Unit cell volume, and bond angles obtained after rietveld refinement for S0, S4, and Z1.

Parameters	**S0**	**S4**	**Z1**
Atomic positions (x,y,z):			
Zn/Sm/Sr	(0,1/4,5/8)	(0,1/4,5/8)	(0,1/4,5/8)
Mo	(0,1/4,1/8)	(0,1/4,1/8)	(0,1/4,1/8)
O	(0.241,0.118,0.047)	(0.236,0.109,0.048)	(0.238,0.109,0.047)
Angles (α, β, γ) in degree	(90, 90, 90)	(90, 90, 90)	(90, 90, 90)
Lattice parameters (Å)			
a	5.397	5.391	5.390
c	12.027	12.012	12.007
Unit cell volume ($Å^3$)	350.33	349.18	348.92
Bond lengths (Å)			
Sr/Sm/Zn-O1	2.597 (3)	2.571 (5)	2.572 (3)
Sr/Sm/Zn-O2	2.588 (3)	2.637 (5)	2.620 (3)
Mo-O	1.766 (3)	1.743 (5)	1.754 (0)
$R_{Factors}$			
R_p	6.87	9.82	8.95
R_{wp}	7.54	10.6	9.72
χ^2	4.29	3.54	4.71

Table 4.2 The crystallite size values of S4, Z1, Z2, and Z3 phosphors.

Sample Code	**Crystallite size (d) in nm**
S4	80
Z1	137
Z2	81
Z3	65

4.3.2 Morphology study

Fig. 4.3 (a) and (b) presents the SEM images of S4 and Z1, respectively. It is examined that the samples show fewer signs of agglomeration and the surface of Z1 microcrystals appears smoother than S4 microcrystals. The S4 and Z1 phosphors have average particle sizes of 1.5 µm and 2.3 µm, respectively. Thus, the average particle size is increased after Zn^{2+} co-doping.

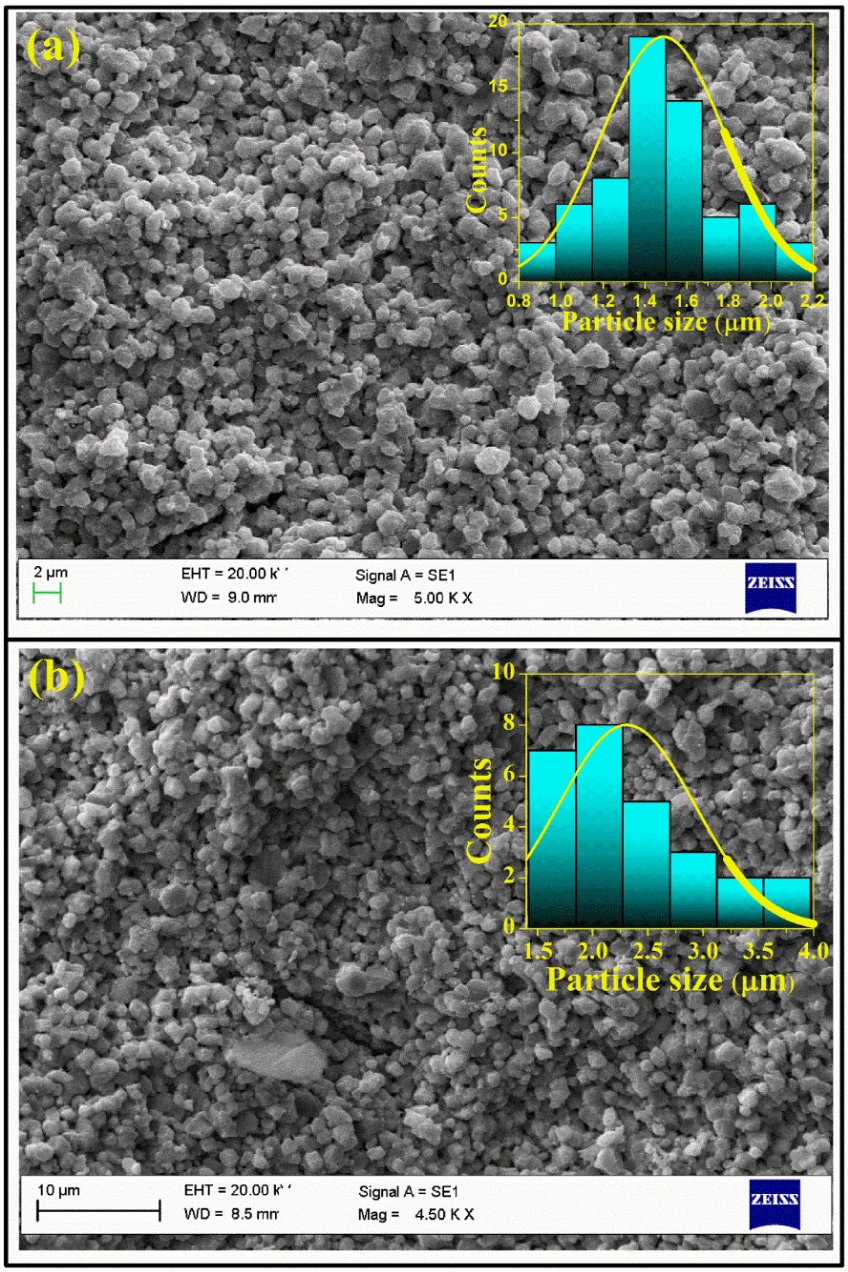

Fig. 4.3 SEM images of **(a)** S4 and **(b)** Z1 with histograms showing the particle size distribution.

4.3.3 FT-IR study

The FTIR spectrum is used to analyze the vibrational modes of the materials. The scheelite-type $SrMoO_4$ has 26 distinct vibrational modes and they are presented by the following equation 4.2:

$$\Gamma = A_1(\nu_1) + E(\nu_2) + F_2(\nu_3) + F_2(\nu_4). \quad (4.2)$$

The Raman active vibrational modes are represented by $A_1(\nu_1)$ and $E(\nu_2)$, whereas the infrared active modes are represented by $F_2(\nu_3, \nu_4)$ [145,146]. The transmittance mode FTIR spectra of S0, S4, and Z1 phosphors are represented in Fig. 4.4.

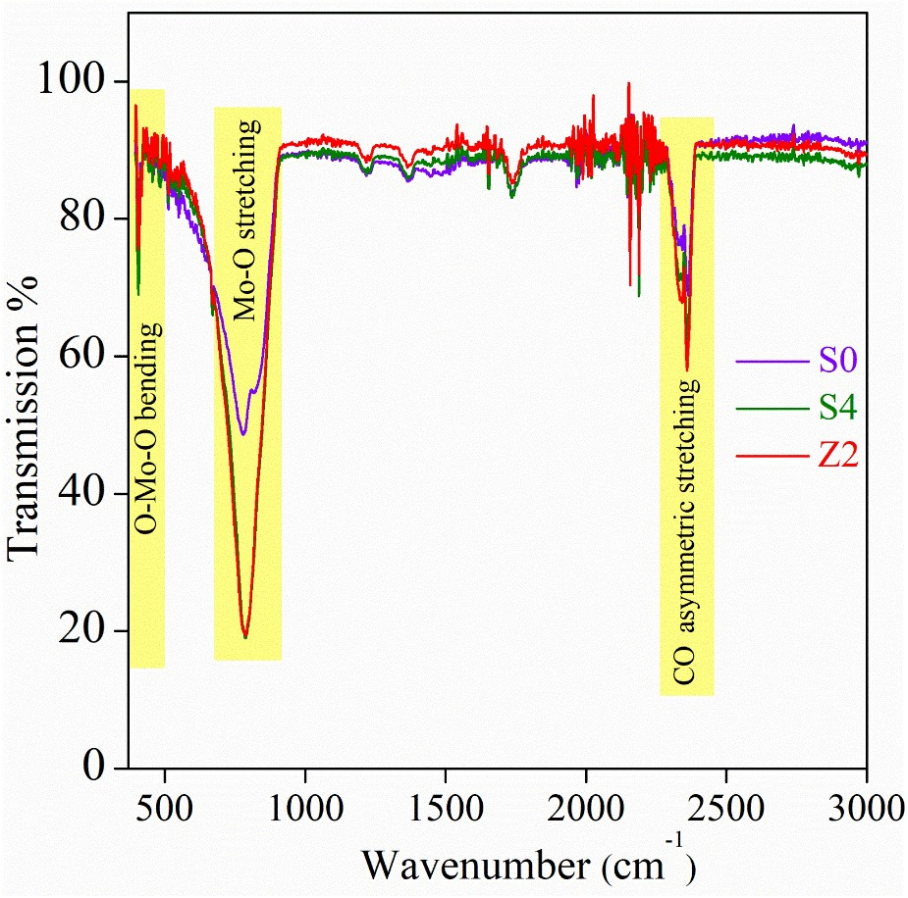

Fig. 4.4 FTIR spectra of S0, S4, and Z1 samples in transmittance mode.

The vibrational band from 548 cm^{-1} to 909 cm^{-1} represents the F_2 (ν_3) antisymmetric stretched vibrations. This intense broadband is dedicated to Mo—O stretching in $[MoO_4]^{2-}$

tetrahedra of $SrMoO_4$. The vibrational band around 405 cm^{-1} is accredited to the F_2 (v_4) bending vibrational mode. This less intense band originates from the bending of O—Mo—O bonds in $[MoO_4]^{2-}$ tetrahedra of $SrMoO_4$ [145,146]. The band from 2310 cm^{-1} to 2380 cm^{-1} corresponds to the CO asymmetric stretching [141]. In our study, we have not observed any deviation in the vibration bands due to doping. The detected vibrational bands of $[MoO_4]^{2-}$ tetrahedral clusters of $SrMoO_4$ support XRD results and manifests the formation of crystalline phase for S0, S4, and Z1 samples.

4.3.4 XPS Study

The elemental presence and validation of their oxidation state in the S4 and Z1 samples are done with the help of the XPS study. The acquired XPS data of all elements were charge corrected for C1s (~284.6 eV). The survey scans of the S4 and Z1 phosphors depicted the Fig. 4.5 (a) confirm the presence of all prominent peaks corresponding to Sr, Mo, O, and Sm. All peaks in the survey scan are assigned as per the national institute of standard technology (NIST) XPS database [147]. The survey scan also validates that there is no additional impurity present in the sample other than carbon. The carbon peak is present because of its absorption on the surface of the sample during air exposure. The XPS binding energy spectrums of Sr (3d), Mo (3d), O (1s), Sm (3d), and Zn (2p) for the S4 and Z1 samples, are presented in Fig. 4.5 (b) to Fig. 4.5 (f) and corresponding binding energies are tabulated in Table 4.3. As depicted in Fig. 4.5 (b), the two bands corresponding to $3d_{3/2}$ and $3d_{5/2}$ levels of Sr ion are centered at ~134.3 eV and ~132.7 eV [129]. The binding energy curve of strontium validates the +2 oxidation state of strontium in the S4 and Z1 phosphors. Fig. 4.5 (c) depicts the XPS spectra of the Mo 3d core level with the observed peaks centered at ~235.2 eV and ~232 eV. These peaks are ascribed to the core level binding energy of Mo^{6+} $3d_{3/2}$ and Mo^{6+} $3d_{5/2}$ levels, respectively, which indicates that molybdenum is in a +6 oxidation state in the S4 and Z1 phosphors [112,129]. Fig. 4.5 (d) shows the peak centered at

~529.9 eV which corresponds to O 1s. The asymmetric O 1s peak is deconvoluted into two peaks. For Z1 phosphor the peaks are at ~529.8 eV and ~530.9 eV and for S4 phosphor they are at ~529.5 eV and ~530.3 eV. The peak at lower binding energy (B.E) is attributed to lattice oxygen and the peak at higher B.E is due to the surface adsorbed oxygen [112]. The binding energy curve of samarium ions for S4 and Z1 samples are presented in Fig. 4.5 (e). As depicted in Fig. 4.5 (e), the peak of two bands is observed at ~1109.5 eV and ~1082.6 eV which are ascribed to $3d_{3/2}$ and $3d_{5/2}$ core levels of samarium, respectively [112]. The XPS spectra validate the +3 oxidation state of samarium ions. The Zn 2p core-level XPS spectrum for Z1 phosphor is depicted in Fig. 4.5 (f). The peak of the band is at 1020.8 eV and is ascribed to Zn $2p_{3/2}$ core level and confirms the presence of Zn ions in the +2 oxidation state in Z1 phosphor [148]. The details of the XPS spectra confirm the presence and oxidation states of S4 and Z1 phosphors.

Table 4.3 The obtained binding energies of all the elements present in S4 and Z1 samples from their respective XPS spectrums.

Elements	**State**	**B.E. (eV)**	
		S4	**Z1**
Sr 3d	Sr^{+2} $3d_{3/2}$	134.03	134.3
	Sr^{+2} $3d_{5/2}$	132.3	132.7
Mo 3d	Mo^{+6} $3d_{3/2}$	234.8	235.2
	Mo^{+6} $3d_{5/2}$	231.7	232
O 1s	$O^{-2}{}_1$ 1s	529.5	529.8
	$O^{-2}{}_2$ 1s	530.3	530.9
Sm 3d	Sm^{+3} $3d_{3/2}$	1109.5	1109.5
	Sm^{+3} $3d_{5/2}$	1082.6	1082.6
Zn 2p	Zn^{+2} $2p_{3/2}$	-	1020.8

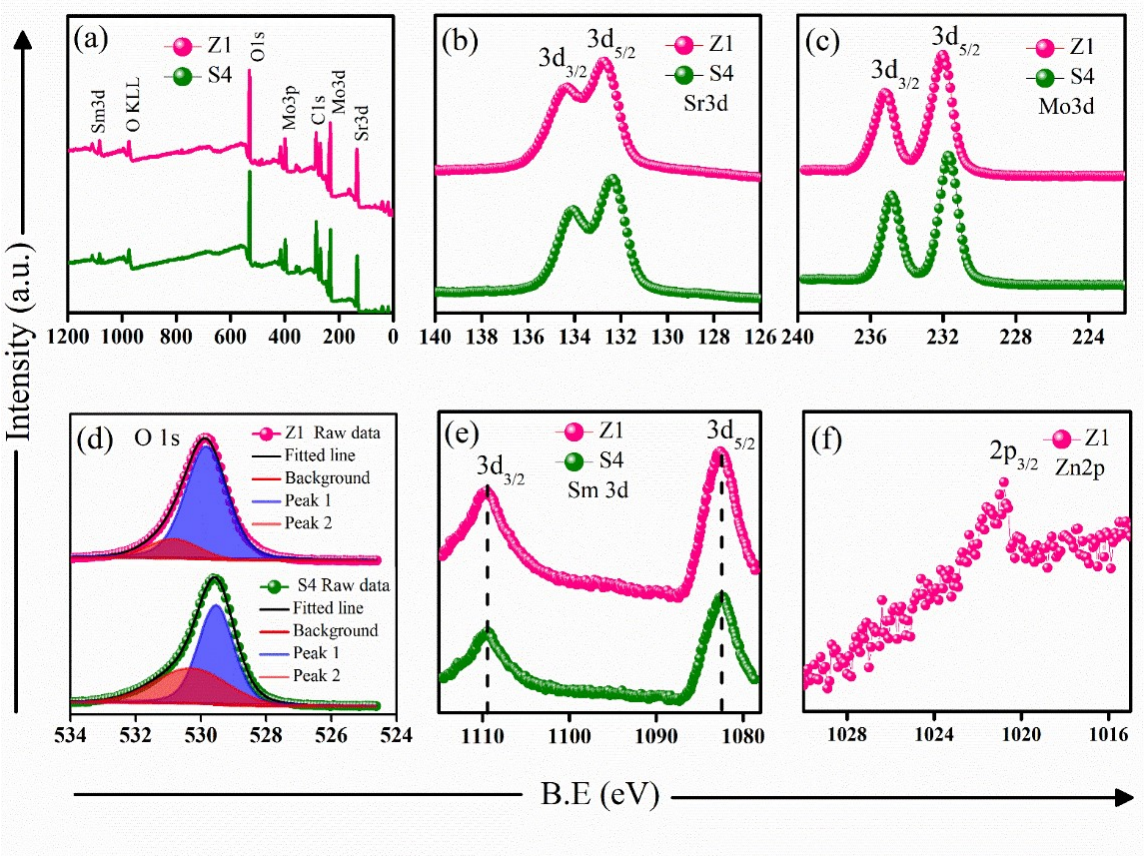

Fig. 4.5 (a) XPS Survey scan for S4 and Z1. XPS high resolution **(b)** Sr 3d, **(c)** Mo 3d, **(d)** O 1s, **(e)** Sm 3d spectra of S4 and Z1. (f) XPS spectra of Zn 2p for Z1 sample.

4.3.5 Absorption study

Fig. 4.6 (a) presents the UV-Vis absorption spectrum of the S series and Z1 phosphor. The charge transfer broadband (CTB) for S0 is observed at 264 nm and it is associated with the charge transfer from O^{2-} to Mo^{6+} ions [20]. The absorption CTB for the Sm^{3+} doped phosphors is shifted slightly towards the higher wavelength (lower energy), as in the case of Sm^{3+} doped phosphors both $O^{2-} \rightarrow Mo^{6+}$, and $O^{2-} \rightarrow Sm^{3+}$ charge transfer process contribute to the absorption broadband [113]. A small characteristic peak corresponding to $^6H_{5/2} \rightarrow {}^4F_{7/2}$ transition of Sm^{3+} ions is observed at 404 nm in the spectrum of Sm^{3+} doped phosphors and Z1 phosphor [23,24].

The energy gap (E_g) is calculated using the following Wood and Tauc formula [130],

$$\alpha h\nu = A(h\nu - E_g)^n, \tag{4.3}$$

Where α denotes the absorption coefficient, $h\nu$ represents photon energy and the nature of electronic transitions establishes the value of n. The $SrMoO_4$ exhibit direct allowed electronic transitions, therefore n=1/2 [24,113]. The Tauc plot of all the phosphors is presented in the inset of Fig. 4.6 (a). The E_g is approximated by extrapolating the linear part of the Tauc plot, where the x-intercept for $(\alpha h\nu)^2$=0 gives the value of E_g in eV. The approximate value of E_g for S0 is 4.11 eV, and is in good agreement with our earlier report [23]. The value of E_g is reduced as we incorporate Sm^{3+} ions in the $SrMoO_4$ matrix. The reduction in bandgap is because of the formation of intermediate defect energy levels of Sm^{3+} ions, which results in the flow of electrons from O^{2-} to intermediate Sm^{3+} orbitals.

The emergence of the defect levels within the bandgap of $SrMoO_4$, as a result of Sm^{3+} and Zn^{2+} doping, can be substantiated by examining the variation in Urbach energy (E_u). The relation between α and E_u is given by the following equation 4.4 [23].

$$\alpha = \alpha_0 e^{\left(\frac{h\nu}{E_u}\right)} \tag{4.4}$$

Where, α_0 is a constant and $h\nu$ and α represent photon energy and the absorption coefficient, respectively. The ln (α) vs $h\nu$ plot for S0 is shown in Fig. 4.6 (b). The reciprocal of the slope of the linear part of ln (α) vs $h\nu$ plot gives the value of E_u. The E_u variation is depicted in the inset of Fig. 4.6 (b). The E_u increases after Sm^{3+} and Zn^{2+} doping which validates the formation of defect states within the bandgap of $SrMoO_4$ [131].

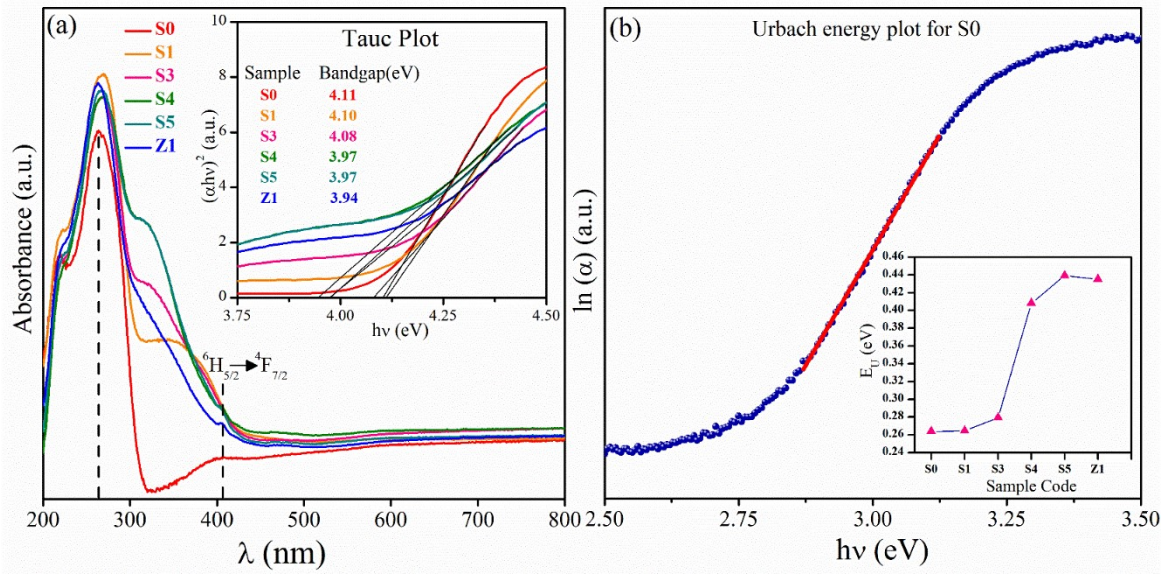

Fig. 4.6 (a) UV-Vis absorption graphs of $SrMoO_4$, Sm^{3+} doped $SrMoO_4$, and Z1 phosphors. The Tauc plot is presented in the inset. **(b)** Urbach energy plot for S0. Inset showing the Urbach energy variation.

4.3.6 Photoluminescence study

PLE spectrum of S0 monitored at 497 nm emission wavelength is depicted in Fig. 4.7 (a).

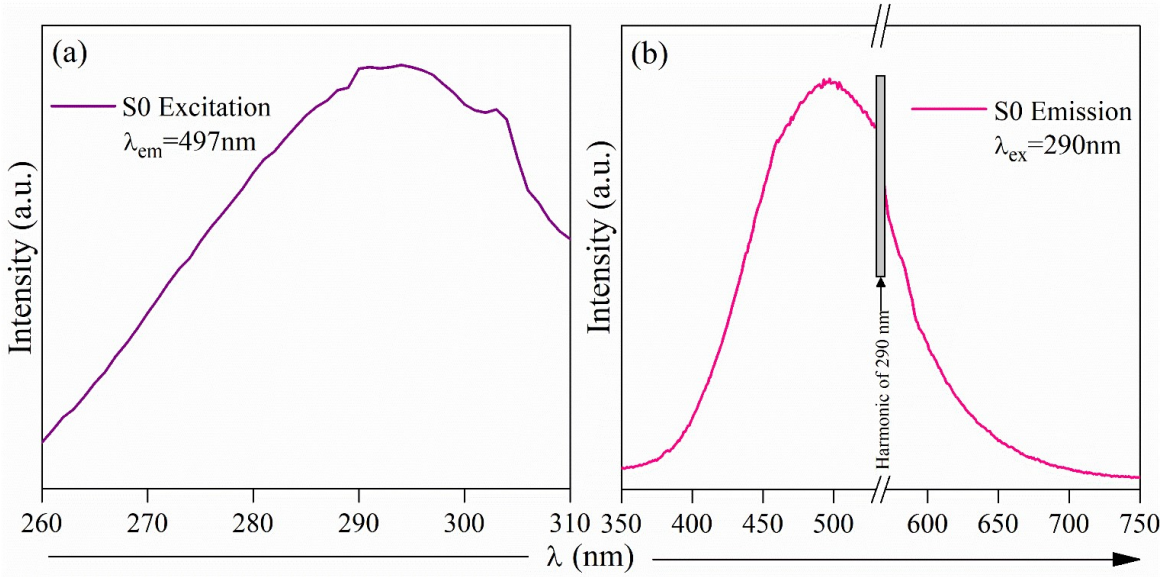

Fig. 4.7 (a) PLE spectrum of S0 recorded at 497 nm emission wavelength. **(b)** PL spectrum of S0 in the wavelength range 350-750 nm and monitored at 290 nm excitation wavelength.

A ligand-metal charge transfer (LMCT) broadband, is observed around 290 nm. The $O^{2-} \rightarrow Mo^{6+}$ charge transfer in $[MoO_4]^{2-}$ groups of $SrMoO_4$ results in the LMCT band observed in the PLE spectrum [113].

Fig. 4.8 (a) depicts the PLE spectrum of Sm^{3+} doped $SrMoO_4$ phosphors. The PLE spectrum of the Sm^{3+} doped series was examined at 644 nm accredited to $^4G_{5/2} \rightarrow {}^6H_{9/2}$ emission transition of Sm^{3+} ion.

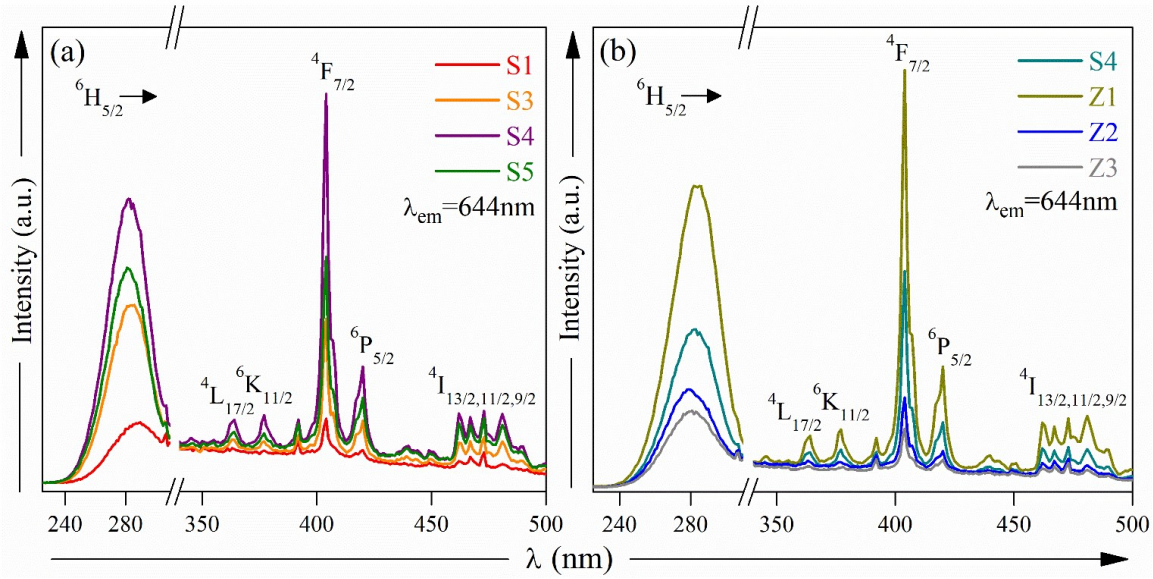

Fig. 4.8 (a) Comparative PLE spectrum of Sm^{3+} doped $SrMoO_4$ phosphors. **(b)** Comparative PLE spectrum of S4 and Zn^{2+} co-doped samples.

The broadband observed for the Sm^{3+} doped series is deconvoluted and depicted in Fig. 4.10 (b). The broadband is centered at 287 nm (4.3 eV) and the deconvoluted two peaks are centered at 290 nm (4.27 eV) and 280 nm (4.4 eV), ascribed to LMCT band and CTB resulting from the charge transfer from full 2p orbital of O^{2-} to the partially filled orbital of the Sm^{3+} ions, respectively [113]. Some characteristic peaks accredited to f-f transitions of Sm^{3+} ions are also observed in the PLE spectrum. These peaks are at 364 nm ($^6H_{5/2} \rightarrow {}^4L_{17/2}$), 377 nm ($^6H_{5/2} \rightarrow {}^6K_{11/2}$), 404 nm ($^6H_{5/2} \rightarrow {}^4F_{7/2}$), 420 nm ($^6H_{5/2} \rightarrow {}^6P_{5/2}$), and 462-481 nm ($^6H_{5/2} \rightarrow {}^4I_{13/2,11/2,9/2}$) [114,116]. It is observed that the excitation peak intensity is maximum for S4 and then decreases with further Sm^{3+} doping. The peak at 404 nm ($^6H_{5/2} \rightarrow {}^4F_{7/2}$) has the

strongest intensity. Thus, the strongest excitation peak lies in the near UV region, which is essential for white light LED device application because it overlaps with the PL spectrum of commercial blue LED chips required in fabricating white light LEDs. Fig. 4.8 (b) depicts the comparison between the PLE spectrum of S4 and Zn^{2+} co-doped samples. The broadband spectrum and the excitation peak intensity at 404 nm peak ($^6H_{5/2} \rightarrow {}^4F_{7/2}$) is maximum for Z1. The overall enhancement in the 404 nm peak is about 93.5% after 1% Zn^{2+} co-doping in the 4 % Sm^{3+} doped phosphor.

Fig. 4.7 (b) depicts the PL spectrum of S0 in the wavelength range 350-750 nm and monitored at 290 nm excitation wavelength. Broadband centered on 497 nm is attributed to the charge transfer from Mo^{6+} to O^{2-} in $[MoO_4]^{2-}$ groups [113]. Fig. 4.9 (a) depicts the PL spectrum of Sm^{3+} doped series in the wavelength range 525-750 nm and monitored at 404 nm excitation wavelength. Some specific emission peaks of Sm^{3+} ion are detected at 562 nm, 597 nm, 645 nm, and 705 nm, which corresponds to $^4G_{5/2} \rightarrow {}^6H_{J/2}$ (J=5, 7, 9, and 11) transitions of Sm^{3+} ion, respectively. All the observed peaks are in good agreement with the previously reported work [109,113,116]. Among all the distinctive emission peaks, the peak at 645 nm corresponding to $^4G_{5/2} \rightarrow {}^6H_{9/2}$ transition has the highest PL intensity. The peak splitting observed at 597 nm ($^4G_{5/2} \rightarrow {}^6H_{7/2}$) is the result of crystal field splitting [113]. The peak at 645 nm ($^4G_{5/2} \rightarrow {}^6H_{9/2}$) is because of ED transition and the local symmetry around Sm^{3+} ions in the $SrMoO_4$ lattice can influence it. The intense ED transition peak (645 nm) manifests that the Sm^{3+} ions sit in a lower symmetry site in the $SrMoO_4$ lattice [127]. The emission peak intensity increases up to 4% Sm^{3+} concentration and then decreases. The decreasing trend of the emission peak intensity is attributed to the high concentration quenching [116]. Therefore, it is concluded that the ideal concentration of Sm^{3+} ion for $SrMoO_4$ host phosphor is 4%. Usually, there are two mechanisms by which the process of quenching among the luminescent centers can be realised. One is the exchange interaction

while the other is electric multipolar interaction. When the wave-functions of the accepter and donor ions overlap after a certain distance, known as the critical distance (R_c), the process is called exchange interaction. This increases the non-radiative energy transfer among the ions and consequently the intensity of the emission peaks decreases. The critical distance between the two Sm^{3+} ions present in the $SrMoO_4$ lattice is estimated using the equation 4.5 [136],

$$R_c = 2\left(\frac{3V}{4\pi x_c N}\right)^{\frac{1}{3}} \tag{4.5}$$

Where unit cell volume of $SrMoO_4$ is denoted by V and from Rietveld refinement analysis, it is estimated to be 349.18 $Å^3$. The critical concentration of Sm^{3+} ions is denoted by x_c, which in our case is 0.04. The maximum number of sites occupied by Sm^{3+} ion is denoted by N, which is 4 for $SrMoO_4$ lattice. The calculated value of R_c is 16.09 Å. The exchange interaction is possible when the critical distance is below 5 Å [24,136]. The calculated value of R_c in our case suggests that the non-radiative energy transfer in $SrMoO_4$ lattice is because of electric multipolar interactions and not due to exchange interaction.

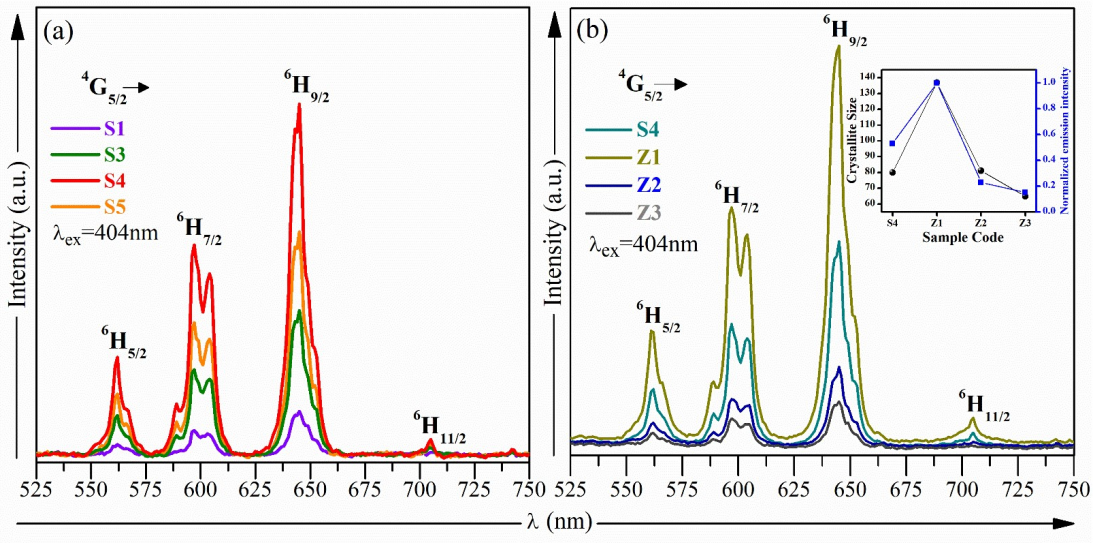

Fig. 4.9 (a) The comparative PL spectrum of Sm^{3+} doped series in the wavelength range 525-750 nm. **(b)** The PL spectrum of Zn^{2+} co-doped samples and S4 in 525-750 nm wavelength range.

Fig. 4.9 (b) shows the comparative PL spectrum of Zn^{2+} co-doped phosphors and S4 monitored at 404 nm excitation wavelength. It is observed that the Z1 phosphor has the maximum PL intensity.

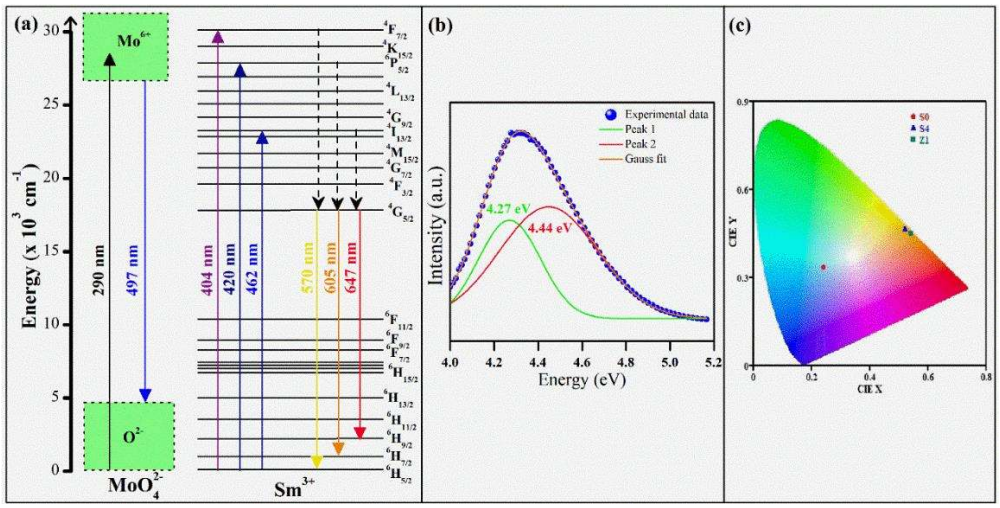

Fig. 4.10 (a) The schematic of an energy transfer mechanism for MoO_4^{2-} groups and Sm^{3+} ions. **(b)** The deconvoluted broadband spectrum of S4. **(c)** CIE coordinates for S0, S4, and Z1 samples are marked in the CIE diagram.

The energy transfer process in Sm^{3+} ions is depicted in Fig. 4.10 (a). The doped and co-doped phosphors are excited with the 404 nm wavelength corresponding to the $^6H_{5/2} \rightarrow {}^4F_{7/2}$ transition of Sm^{3+} ions. The electrons absorb photon energy and jump to the higher energy levels of the Sm^{3+} ions. The electrons then move to the lowest excited level ($^4G_{5/2}$) by partially transferring energy to the lattice. This non-radiative relaxation of the electrons is marked with black dash lines in Fig. 4.10 (a). The electrons finally revert to the ground state via radiative transitions giving characteristic reddish-orange emission. The increase in PL intensity of Z1 is 87.80% as compared to S4. The enhancement in the PL intensity of Z1 is the result of the non-sensitization effect of Zn^{2+} ions. The improvement in the intensity of PL spectra is ascribed to the increase in crystallite size and increase in particle size after Zn^{2+} doping. The XRD study reveals that the crystallinity of the host sample is ameliorated with Zn^{2+} doping. The improved crystallinity contributes toward the PL enhancement as

inferred from the inset of Fig. 4.9 (b). The defect centers present on the surface of the particles operate as quenching centers for the excited ions, as these defects absorb energy and then prompt ions to relax non-radiatively to their ground state. Thus, with the increase in defect centers, the non-radiative relaxation of ions also increases. It is observed that the increased crystallinity helps in increasing the particle size of the phosphors and therefore the surface-to-volume ratio reduces [142]. Since many defect centers are present on the particle surface, the decrease in the surface-to-volume ratio minimizes the interaction between the defect centers and the ions. Therefore, the overall number of radiative ions in the crystallites increases thereby increasing the emission intensity [121,139,142,149]. It is also observed that for the Z1 sample, the intensity of the 404 nm peak in the PLE spectrum is maximum. Therefore, the increased absorption for the Z1 sample is another reason for the increased emission intensity in the Z1 sample. The further increase in Zn^{2+} content prompts Zn^{2+} ions to occupy interstitial sites, which creates defects in the crystal and therefore leads to luminescence quenching.

4.3.7 PL Decay analysis

The PL decay curves of S4 and Z1 phosphors recorded upon 404 nm excitation ($^6H_{5/2} \rightarrow {}^4F_{7/2}$) and 645 nm emission ($^4G_{5/2} \rightarrow {}^6H_{9/2}$) are presented in Fig. 4.11 (a) and (b), respectively. The decay curves were examined by fitting them with the bi-exponential function [23],

$$I(t) = I_0 + B_1\, exp\left(-\frac{t}{\tau_1}\right) + B_2\, exp\left(-\frac{t}{\tau_2}\right) \qquad (4.6)$$

Where intensity after t seconds is denoted by I and the background intensity after prolonged excitation is denoted by I_0; τ_1 denotes fast decay time and τ_2 denotes slow decay time; B_1 and B_2 are the fitting constants. The following relation is used to evaluate the average lifetime [23]:

$$\tau_{avg} = (A_1\tau_1^2 + A_2\tau_2^2)/(A_1\tau_1 + A_2\tau_2) \quad (4.7)$$

Using the above equation 4.7, the average lifetime of the $^4G_{5/2}$ level of the Sm^{3+} ion for S4 and Z1 is 732.66 µs and 761.84 µs, respectively.

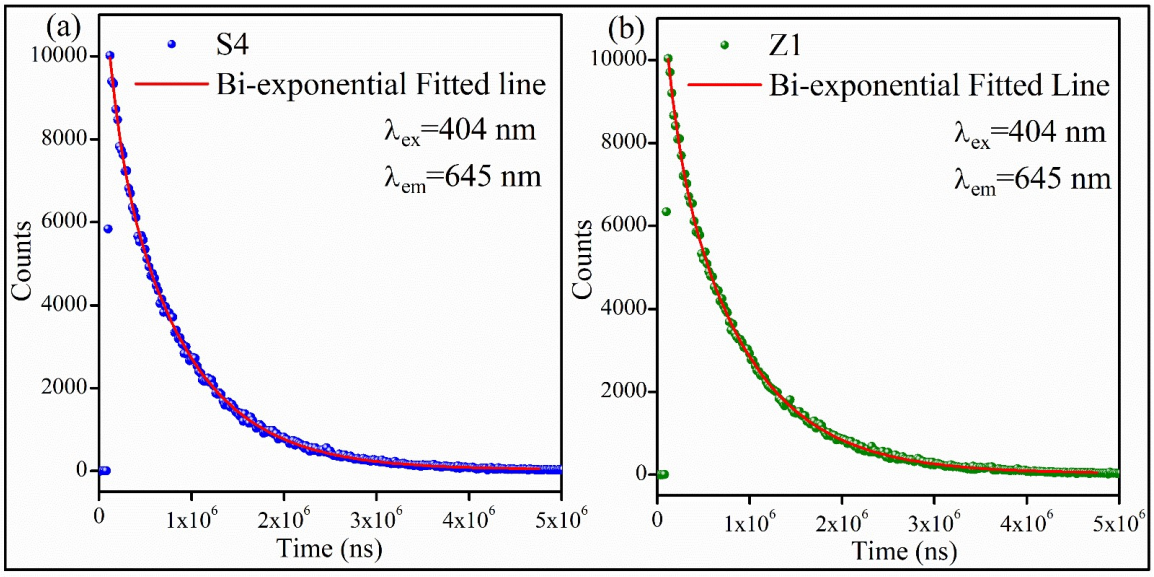

Fig. 4.11 PL decay curves of **(a)** S4 and **(b)** Z1 samples, recorded upon 404 nm excitation and 645 nm emission.

The lifetime of Sm^{3+} ions is increased after 1% Zn^{2+} ions co-doping. The increased lifetime is attributed to the improved crystallinity in the Z1 phosphor. The defect centers are the active quenching centers because the emitting ions lose part of their energy to these defect centers and relax to the ground state non-radiatively. The improvement in crystallinity in the Z1 phosphor is an indication of the reduction of defect centers. Thus, by improvement in crystallinity, the probability of non-radiative relaxation of the emitting ions is reduced and the average lifetime of emitting ions is increased [139,140,142,150]. It is also inferred that the average particle size is increased after 1% Zn^{2+} co-doping. The increase in particle size reduces the surface-to-volume ratio and the overall grain boundaries. The defect centers are comparatively larger on the surface of the particles and with the decrease in surface area and the overall grain boundaries, the number of emitting ions interacting with them also

decreases, and the average lifetime of emitting ions increases [139,150]. The analysis of decay curves also supports the increase in the emission intensity for 1% Zn^{2+} co-doped phosphor.

4.3.8 CIE and CCT study

The Commission Intentional de I'eclairage (CIE) chromaticity coordinates for S0, S4, and Z1 obtained from their respective room temperature PL spectrum are plotted in the CIE diagram depicted in Fig. 4.10 (c). The obtained CIE coordinates (x, y) for S4 and Z1 are (0.519, 0.466) and (0.541, 0.448), respectively. As presented in the CIE diagram, the overall emission of the prepared phosphors is reddish-orange. The CIE coordinates are shifted more towards the red region after Zn^{2+} doping.

The value of color correlated temperature (CCT) is estimated using the following McCAMY's expression [151].

$$CCT = 5520.33 - 6823n + 3525n^2 - 449n^3 \quad (4.8)$$

The CCT is calculated from the third-degree polynomial given by McCamy's method. The polynomial equation is derived from the assumption that all isothermal lines are interconnected at a fixed point in the chromaticity diagram. Where x and y are the CIE coordinates, x_e and y_e are the chromaticity epicenter (0.338, 0.186), and $n = \frac{(x-x_e)}{(y-y_e)}$ is the inverse slope line. The calculated CCT from the above equation for S4 and Z1 is 2457 K and 2142 K, respectively.

4.3.9 Temperature-dependent PL analysis

The investigation of the thermal stability of the phosphor is vital for its technological utilization. In this regard, we have analyzed the thermal quenching phenomenon in the Z1 sample. Fig. 4.12 (a) depicts the TDPL spectrum of Z1 phosphor in the temperature range of 303 – 623 K. It is evident that with rising temperature there is a gradual decrease with a

slight broadening in the PL intensity. As shown in Fig. 4.12 (a) and Fig. 4.13 (a), the emission intensity of the 562 nm peak weakens less slowly as compared to the two prominent peaks at 597 nm and 645 nm. The integrated emission intensity decreases as the operating temperature increases from 303K to 623K. At 423K, the emission intensity is 69% of the intensity at 303 K (Fig. 4.13 (b)). Therefore, there is a 31% loss of emission intensity as compared to room temperature emission. The loss at 423K is lower than the commercial $Y_3Al_5O_{12}:Ce^{3+}$ phosphor and some of the other reported phosphors [152–154].

The mechanism of luminescence thermal quenching can be elucidated by the configurational coordinate diagram presented in Fig. 4.12 (b), where U_e and U_g denote the excited and ground state parabola, respectively. The U_e and U_g parabolas intersect at point A and the energy barrier between point A and the minimum of the U_e parabola is the thermal activation energy *(*$\Delta \boldsymbol{E}$) required for thermal quenching. At first, the electrons in the U_g state absorb incident photon energy (photoexcitation) and jump to the excited state (U_e). At room temperature, the electrons are relaxed to the equilibrium position in the U_e state by partially transferring energy to spin-lattice vibration and following the non-radiative (1) path. Finally, electrons revert to the ground state via radiative transition by following the (2) path. The energy of the emitted photons is usually lower than the energy required for exciting activator ions because of the energy involved in the lattice relaxation of the activator ion to reach the excited steady-state. When the temperature is raised, the lattice vibrations are strengthened which increases the thermally active phonons. After coupling with the thermally active phonons, the energy of the excited electrons at the bottom of the U_e state can approach the crossover point A. These electrons revert to the ground state non-radiatively by following the path (3). With increasing temperature, the electron-phonon interaction increases and more electrons cross $\Delta \boldsymbol{E}$ barrier, thereby relaxing non-radiatively

to the ground state [155]. Any remarkable shift in peak positions is not observed, which is desirable for lighting applications.

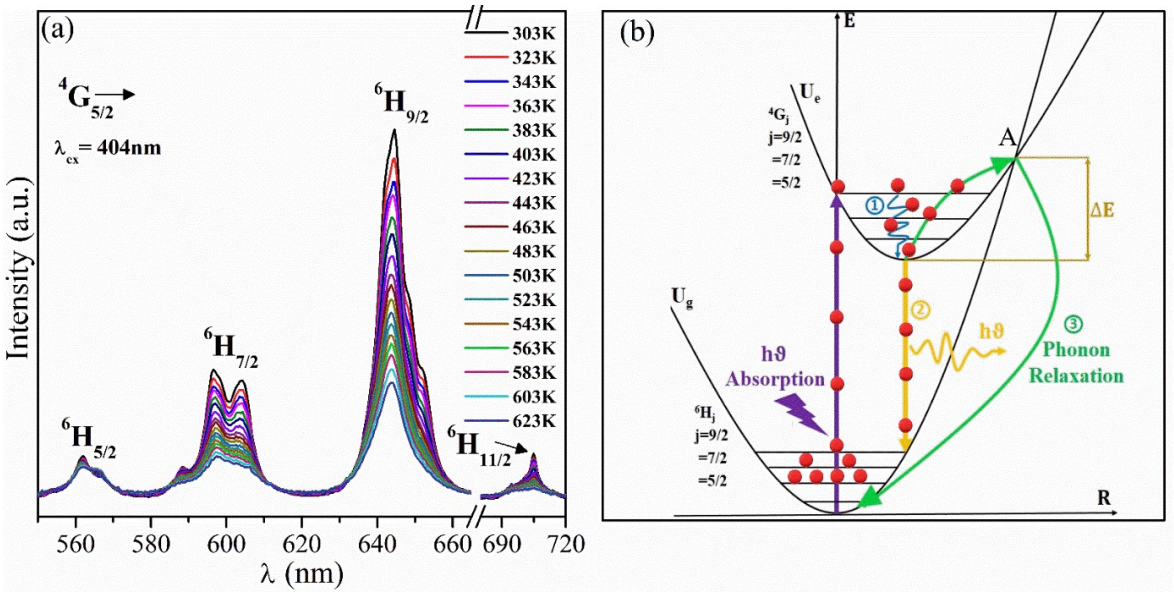

Fig. 4.12 (a) Temperature-dependent PL spectra of Z1 phosphor. **(b)** Configurational coordinate diagram for understanding thermal quenching phenomenon in Z1 phosphor.

The influence of the thermal quenching mechanism on the emission spectra can be further examined by evaluating the ΔE from the following Arrhenius equation 4.9 [152],

$$I_T = \frac{I_0}{1+Ae^{(-\Delta E/kT)}} \tag{4.9}$$

Where k denotes the Boltzmann constant (8.629 **x** 10^{-5} eV/K), I_0 represents the emission intensity at 303K, I_T is the emission intensity at temperature T, and A is the constant frequency factor. The $\ln\left(\frac{I_0}{I_T}-1\right)$ vs 1/kT plot, as shown in Fig. 4.13 (c), is linearly fitted and the slope of the fitted line gives the value of ΔE. The obtained value of ΔE is 0.17 eV, which is higher than some of the Sm^{3+} doped phosphors [2,152,153,156–158]. The comparatively high ΔE value illustrates that Z1 phosphor is thermally stable. The good thermal stability of the phosphor is required to avoid overall emission color shifting. The influence of rising temperature on the emission color is explored by examining the CIE chromaticity

coordinates of the Z1 phosphor at different temperatures. As depicted in Fig. 4.13 (d), there is no remarkable change in the color coordinates under high temperatures. This conclusion is important as stable emission color under working temperatures is desirable for the application of the near UV wLED application.

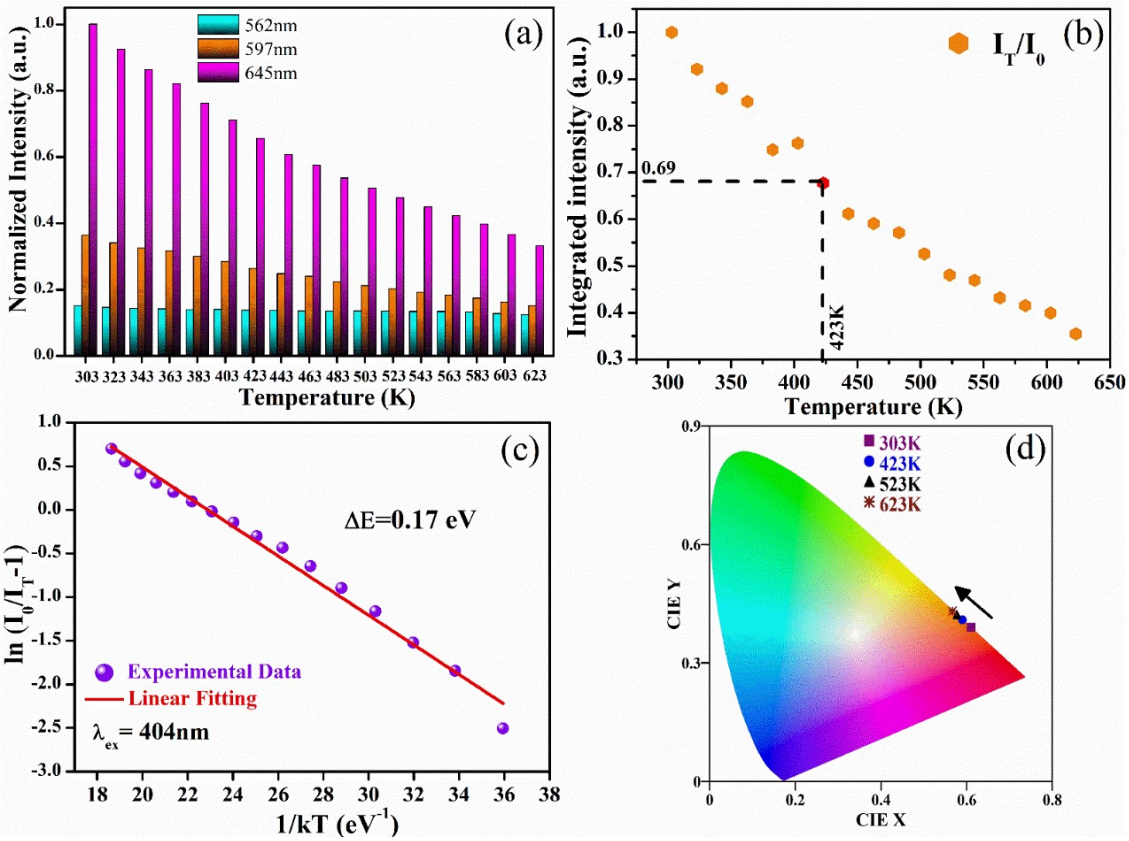

Fig. 4.13 (a) Bar diagram depicting intensity variation of three major peaks with increasing temperature. **(b)** Normalized integrated intensity plot as a function of temperature for Z1 phosphor. **(c)** ln $((I_0/I_T)-1)$ vs. 1/kT plot for the determination of activation energy. **(d)** CIE chromaticity diagram depicting variation in CIE coordinates with temperature for Z1 phosphor.

4.4 Conclusions

In this work, Sm^{3+} and Zn^{2+} doped $SrMoO_4$ phosphors were developed by a lucrative auto-combustion process. The Rietveld refinement of XRD patterns validates the tetragonal crystal structure. The FTIR spectroscopic study validates the existence of vibrational bands corresponding to $[MoO_4]^{2-}$ tetrahedral clusters present in $SrMoO_4$. The absorption spectroscopy reveals that the bandgap of $SrMoO_4$ phosphors is reduced after Sm^{3+} and Zn^{2+} doping, which results from the formation of defect levels within the bandgap. The increase in the Urbach energy after Sm^{3+} and Zn^{2+} doping validate the formation of intermediate defect states. Upon 404 nm excitation, the Sm^{3+} doped phosphors give distinctive emission lines with the highest intensity peak at 645 nm ascribed to $^4G_{5/2} \rightarrow {}^6H_{9/2}$ transition. The emission intensity of Sm^{3+} doped phosphors is further enhanced by 87.80 % after 1% Zn^{2+} co-doping. The lifetime of reddish-orange emitting Sm^{3+} ions is increased after 1 % Zn^{2+} ions co-doping. The analysis of decay curves also supports the increase in the emission intensity for 1 % Zn^{2+} co-doped phosphor**.** The temperature-dependent PL analysis reveals that PL emission decays by 31 % at 423 K (150 ℃) and the thermal activation energy was calculated to be 0.17 eV. Our study reveals that Zn^{2+} co-doping improves crystallinity by favoring crystallite growth and also increases average particle size. Our study ascertains that overall improvement in crystallinity and increased average particle size, resulting from Zn^{2+} co-doping, contribute towards the enhancement of emission intensity.